### Title

Diurnal cross-shore thermal exchange on a tropical forereef




### Journal

Journal of Geophysical Research - Oceans, 119(9)

### ISSN

2169-9275



### Authors

Molina, L
Pawlak, G
Wells, JR
et al.



### Publication Date

2014-09-01

### DOI

10.1002/2013jc009621

Peer reviewed

AGU PUBLICATIONS

JGR

Journal of Geophysical Research: Oceans

RESEARCH ARTICLE

10.1002/2013JC009621

# Diurnal cross-shore thermal exchange on a tropical forereef

**L. Molina[1], G. Pawlak[2], J. R. Wells[1], S. G. Monismith[3], and M. A. Merrifield[4]**

[1]Department of Ocean and Resources Engineering, University of Hawaii at Manoa, Honolulu, Hawaii, USA, [2]Department of Mechanical and Aerospace Engineering, University of California San Diego, San Diego, California, USA, [3]Department of Civil and Environmental Engineering, Stanford University, Stanford, California, USA, [4]Department of Oceanography, University of Hawaii at Manoa, Honolulu, Hawaii, USA

**Key Points:**
- Thermal exchange can contribute to cross-shore transport on open shorelines
- Cross-shore variability is linked to heat flux, alongshore currents, and wind
- Alongshore nonuniformity has important implications on the cross-shore flow

**Correspondence to:**
G. Pawlak,
pawlak@ucsd.edu

**Citation:**
Molina, L., G. Pawlak, J. R. Wells, S. G. Monismith, and M. A. Merrifield (2014), Diurnal cross-shore thermal exchange on a tropical forereef, *J. Geophys. Res. Oceans*, *119*, doi:10.1002/2013JC009621.

Received 21 NOV 2013
Accepted 25 AUG 2014
Accepted article online 2 SEP 2014

**Abstract** Observations of the velocity structure at the Kilo Nalu Observatory on the south shore of Oahu, Hawaii show that thermally driven baroclinic exchange is a dominant mechanism for cross-shore transport for this tropical forereef environment. Estimates of the exchange and net volume fluxes are comparable and show that the average residence time for the zone shoreward of the 12 m isobath is generally much less than 1 day. Although cross-shore wind stress influences the diurnal cross-shore exchange, surface heat flux is identified as the primary forcing mechanism from the phase relationships and from analysis of momentum and buoyancy balances for the record-averaged diurnal structure. Dynamic flow regimes are characterized based on a two-dimensional theoretical framework and the observations of the thermal structure at Kilo Nalu are shown to be in the unsteady temperature regime. Diurnal phasing and the cross-shore momentum balance suggest that turbulent stress divergence is an important driver of the baroclinic exchange. While the thermally driven exchange has a robust diurnal profile in the long term, there is high temporal variability on shorter time scales. Ensemble-averaged diurnal profiles indicate that the exchange is strongly modulated by surface heat flux, wind speed/direction, and alongshore velocity direction. The latter highlights the role of alongshore variability in the thermally driven exchange. Analysis of the thermal balance in the nearshore region indicates that the cross-shore exchange accounts for roughly 38% of the advective heat transport on a daily basis.

## 1. Introduction

Nearshore hydrodynamics affect the transport of nutrients, organisms, heat, and salt, all of which are vital to the health of ecosystems such as coral reefs. Habitat dynamics, including rates of larval dispersion and recruitment, are regulated by the physical processes over the reef and the degree of hydrodynamic closure between adjacent systems [*Hatcher*, 1997; *Cowen and Sponaugle*, 2009]. Cross-shelf fluxes are especially critical to the import of phytoplankton and nutrients and the export of wastes. It has been observed that the rate of nearshore flushing affects the balance between grazing and recycling of organic matter [*Hatcher*, 1997; *Genin et al*., 2009]. For the coastal reef environment at the Kilo Nalu Observatory (KNO) on the south shore of Oahu, Hawaii, the cross-isobath flow is vital not only to the reef ecosystem, but also has implications for nearshore water quality in this densely populated area [*Paul et al*., 1997; *Kellogg et al*., 1995].

The mechanisms that drive cross-shore flow are numerous and depend greatly on shelf width, bathymetry, and stratification. On continental shelves, alongshore winds drive upwelling and Ekman transport on the mid and outer shelf regions [*Huyer*, 1976]. *Symonds and Gardiner-Garden* [1994] have shown that surface cooling can drive significant buoyancy-driven cross-shelf exchange, such as on the southeastern coast of Australia. On inner continental shelves, *Fewings et al*. [2008] found that cross-shelf winds are the main forcing mechanism of the cross-shelf currents, driving a two layer exchange. Waves and stratification were of secondary importance, regulating the strength and structure of the velocity profile. Surface waves can be important for some settings in driving mean flow [*Hench et al*., 2008] and Stokes drift [*Monismith and Fong*, 2004] for nearshore coastal circulation. Internal tidal bores, which bring in colder, saltier water from offshore, can play an important role in regulating temperature over a reef as well as bringing dissolved and suspended materials up from subthermocline waters [*Leichter et al*., 1996].

Buoyancy-driven flow associated with surface heat and salt fluxes has also been studied around atolls [e.g., *Boden*, 1952], in the Red Sea [*Phillips*, 1966], on continental shelves [*Symonds and Gardiner-Garden*, 1994],

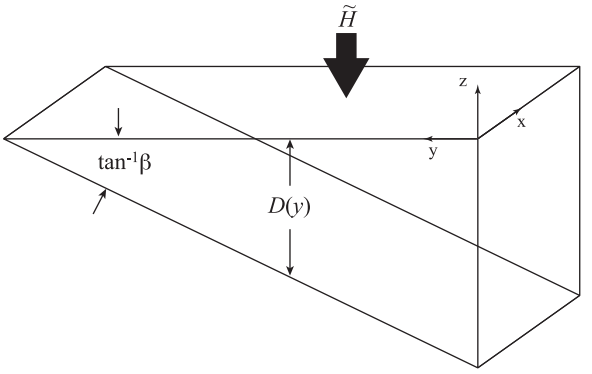


**Figure 1.** Idealized wedge geometry and coordinate system. Here $\beta$ is the bottom slope, $D$ is the depth, and $\tilde{H}$ is the surface heat flux.

and over a fringing reef [*Monismith et al.*, 2006]. The fundamental problem of buoyancy-driven flow on a slope has received much attention in the context of lakes and reservoirs [*Horsch and Stefan*, 1988; *Monismith et al.*, 1990; *Fer et al.*, 2002]. The theoretical framework for these flows has been established for the steady state flow response [*Sturman et al.*, 1999], the transient response to steady forcing [*Lei and Patterson*, 2002, 2005], and unsteady limits [*Farrow and Patterson*, 1993; *Farrow*, 2004]. For the slope case, the basic flow pattern associated with surface cooling leads to flow offshore at depth, compensated by onshore flow at the surface with the opposite flow for surface heating. Transient responses can also lead to cross-shore convergence/divergence fronts with associated strong vertical flows [*Farrow and Patterson*, 1993].

We present observations at KNO that indicate that thermally driven flows are a key mechanism for cross-shore exchange for a fringing reef environment on the south shore of Oahu, Hawaii. Kilo Nalu is located in a fringing reef between the popular beaches of Ala Moana and Waikiki and the industrial port at Honolulu Harbor. Previous research has shown that the currents in this area are mainly regulated by the $M_2$ tide that drives flow along isobaths [*Pawlak et al.*, 2009]. We will show that baroclinic flow associated with surface heat fluxes contributes significantly to the weaker cross-shore currents at KNO. In section 2, we describe the basic problem and its associated theoretical framework. Observational data are presented in section 3. The relative importance of the thermally driven flow is assessed in section 4 along with analyses of momentum and buoyancy balances and of the role of multiple forcing mechanisms in the high variability observed. Finally, results are summarized and interpreted in section 5.

## 2. Background

In order to examine the dynamics of thermally driven baroclinic exchange flow, the physical problem can be idealized as a two-dimensional wedge with unit width (Figure 1), with a cross-shore slope $\beta$. As heat flux is applied uniformly to the surface, shallower waters heat and cool more rapidly than the deeper waters. Thus, in the cross-shore direction, a temperature gradient is set up due to the change in depth. During cooling, denser water formed at the surface sinks and flows offshore, and is compensated by a return flow at the surface. The opposite occurs during heating when warmer surface water flows offshore, compensated by an onshore flow at depth.

The cross-shore and vertical momentum equations are given by:

$$\frac{\partial V}{\partial t}+V\frac{\partial V}{\partial y}+W\frac{\partial V}{\partial z}=-\frac{1}{\rho_0}\frac{\partial P}{\partial y}+\frac{\partial}{\partial z}\left(\nu_t\frac{\partial V}{\partial z}\right)-fU \tag{1}$$

and

$$\frac{\partial W}{\partial t}+V\frac{\partial W}{\partial y}+W\frac{\partial W}{\partial z}=-\frac{1}{\rho_0}\frac{\partial P}{\partial z}+\frac{\partial}{\partial z}\left(\nu_t\frac{\partial W}{\partial z}\right)-B \tag{2}$$

Here $U$, $V$, and $W$ are the alongshore, cross-shore, and vertical velocity components, respectively, $P$ is the pressure, $f$ is the Coriolis parameter, and $\rho_0$ is a reference density. For the case where salinity variations are negligible, the buoyancy is given by $B=-\alpha g(T-T_0)$ with $T$, $T_0$, and $\alpha$ being the water temperature, reference water temperature, and thermal expansion coefficient, respectively. We consider alongshore uniform bathymetry so that the two equations describe a two-dimensional flow, allowing for a Coriolis contribution associated with an alongshore velocity component. Including rotational effects thus couples equations (1) and (2) to the alongshore momentum equation:

$$\frac{\partial U}{\partial t}+V\frac{\partial U}{\partial y}+W\frac{\partial U}{\partial z}=-\frac{1}{\rho_0}\frac{\partial P}{\partial x}+\frac{\partial}{\partial z}\left(\nu_t\frac{\partial U}{\partial z}\right)+fV \tag{3}$$

In general, the alongshore flow can be associated with tidal pressure gradients, wind or wave-driven flow, or geostrophic balance. Here we will consider the situation where Coriolis effects are weak, as will be verified later. The alongshore velocity $U$ is thus predetermined by the balance in (3), which we will not address further.

The mechanics of the cross-shore exchange flow can then be described by equations (1) and (2) along with the buoyancy equation,

$$\frac{\partial B}{\partial t}+V\frac{\partial B}{\partial y}+W\frac{\partial B}{\partial z}=\frac{\partial \tilde{F}}{\partial z}+\frac{\partial}{\partial z}\left(\kappa_t\frac{\partial B}{\partial z}\right) \tag{4}$$

and an equation for volume conservation. Here $\tilde{F}(z)$ is the forcing buoyancy flux, with $\kappa$ representing the thermal diffusivity. The equations are obtained by averaging over time scales that are long relative to wave and turbulent times but much shorter than diurnal thermal forcing time scales. We have neglected horizontal diffusion of momentum and heat with the anticipation that cross-shore slopes are generally small (these terms can be shown to be $O(\beta^2)$ [cf. *Farrow and Patterson*, 1993]). The effects of stress due to wind are included via a momentum boundary condition at the surface. In general, the turbulent eddy viscosity, $\nu_t$, in equations (1) and (2) can be associated with a number of mechanisms including bottom-boundary layer turbulence from alongshore currents, wave-driven boundary layer and breaking wave turbulence, surface wind-driven mixing, and cooling-driven convection. The system is forced via the function $\tilde{F}(z)$, which represents the vertical distribution of buoyancy input. The simplest case uses a buoyancy flux at the surface as

$$\tilde{F}(z,t)=-\frac{\alpha g\tilde{H}(t)}{\rho_0 c_p}\delta(z) \tag{5}$$

where $\tilde{H}$ is the surface heat flux, $c_p$ is the heat capacity, and $\delta$ is the Dirac delta function. The forcing function (5) will be appropriate for latent and sensible heat fluxes. For these cases, which apply for cooling regimes, the turbulent diffusion of heat is intricately linked with the forcing via convectively driven mixing. For clear tropical waters, we can expect that radiative heating will be distributed over some depth so that (5) will take the form of an exponentially decaying function of $z$ with a distribution that is a function of water properties. The choice for equation (5) then defines the surface buoyancy boundary condition. The problem is completed by imposing additional boundary conditions at the bottom (zero buoyancy flux, bottom stress) and at the surface (momentum flux equal to the wind stress).

The nature of the flow response at a given cross-shore location, then, depends on the resulting balances in (1) and (4). For most applications of interest, equation (2) reduces to the hydrostatic balance, providing a link between the surface heat flux forcing in (4) and the flow response in (1) via the pressure distribution. Following the work of *Monismith et al.* [2006], the problem can be simplified by examining the various dynamic limits. For (4), two limits are apparent: a steady regime where forcing is balanced by advection and an unsteady regime where the temperature response to the forcing is transient. For the idealized configuration sketched in Figure 1, diffusion will always be dominant within the shallowest portion of the wedge where the depth is comparable to the relevant turbulent length scale. With an assumption of zero heat flux at the seabed, strong turbulent heat diffusion would still require either a depth uniform unsteady temperature response or an advective regime to balance the surface heat flux in (4).

Considering a scaling analysis at a given depth, $D$, the ratio of the advective terms (second and third terms) to the unsteady term (first term) in both (1) and (4) is given by $\hat{V}\beta T_f/D$, where $T_f$ is the forcing period and $\hat{V}$ is a measure of the cross-shore flow velocity. As $D$ increases offshore, the unsteady term will inevitably dominate relative to the advective terms (consistent with a one-dimensional system). For steeper slopes, in shallower depths the steady, advective inertial terms in (1) and (4) can play a more direct role.

In the unsteady limit, the buoyancy balance reduces to $\partial B/\partial t \sim \partial\tilde{F}/\partial z$, so that the local buoyancy response will be given by the integral in time of the heat flux as for a one-dimensional system. For a cyclical variation in heat flux, the temperature will thus lag the forcing by 90°. For the advective regime, i.e., $V\partial B/\partial y \sim \partial\tilde{F}/\partial z$, we expect a thermal response that is in phase with the cyclical surface heat flux.

The phase response for the cross-shore flow relative to the forcing heat flux is more complicated since it depends on the phasing of the cross-shore pressure gradient in (1). Because the thermal regime may vary

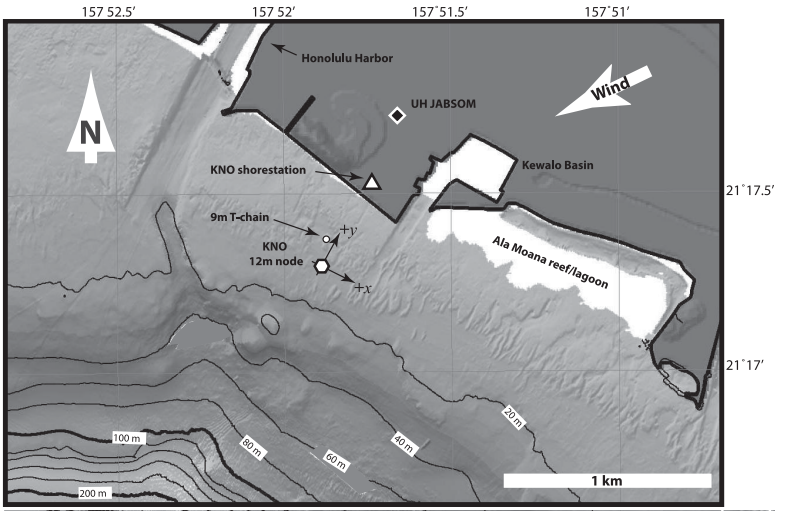


**Figure 2.** Bathymetry for south shore of Oahu including location of KNO 12 m node and 9 m thermistor chain with cross-shore, alongshore coordinate system.

from steady to unsteady with increasing depth, the phasing of the gradient may vary in both space and time. Where the unsteady regime applies throughout the wedge (i.e., low slope), the thermal gradient will follow the temperature and will lag the forcing everywhere by 90°. Within the shallowest region, the diffusive balance requires that the flow will be in phase with the gradient and in quadrature with the heat flux forcing. In the deeper parts of the wedge, the unsteady balance will apply in (4) and the flow should be in quadrature with the gradient and in phase with the heat flux.

Indeed, *Farrow and Patterson* [1993] examined the linearized form of (1)–(4) and found a phase shift between the shallow diffusive region and an unsteady response offshore as described above. The cross-shore phase shift introduced transient convergence/divergence regions with associated down/upwelling regions.

The temporal variation of the turbulent diffusivities in (1)–(4) is more complex. For the cooling case, the surface buoyancy flux affects the flow both by driving a pressure gradient and also by increasing $\nu_t$ via convective turbulence. For the daytime heating case, surface heat flux will tend to diminish vertical transport by increasing stratification. In this case, turbulent transport from other sources (alongshore current-driven bottom stress, wind stress, etc.) is required to drive flow with any substantial vertical extent. In the absence of external turbulence sources, the cross-shore flow would be limited to an offshore surface flow with a thickness determined by the vertical extent of the radiative input.

## 3. Observations

Data were collected at the Kilo Nalu Observatory, located in a fringing forereef environment on the south shore of Oahu, Hawaii (Figure 2) [*Pawlak et al.*, 2009] between Honolulu Harbor to the west and Kewalo Basin and Ala Moana reef and lagoon to the east. The main KNO node at 12 m depth is located approximately 370 m from shore. The slope is fairly constant to the 20 m isobath 700 m from shore, then increases slightly to the 40 m isobath 1 km offshore after which it increases sharply, reaching 100 m depth at 1.5 km. The seabed in the vicinity of the main KNO node is comprised of rough coral reef interspersed with sand channels with widths from O(1 m) to O(10 m).

Cabled instrumentation at the 12 m isobath at KNO included a bottom mounted acoustic Doppler current profiler (ADCP) and a thermistor chain (T-chain). The ADCP (1200 kHz RDI Workhorse) sampled velocity between 2 and 11 m depth at 1 Hz within 0.25 m vertical bins. The bottom moored T-chain (Precision Measurement Engineering Inc.), located about 15 m from the ADCP, consisted of cabled temperature sensors spaced 1 m apart from 5 to 11 m depth, sampling every 3 s. A surface buoy, operated as part of the Pacific Islands Ocean Observing System (PacIOOS), was located about 30 m from the KNO ADCP providing surface temperature and salinity data (Seabird Electronics SBE 37). A second thermistor chain was deployed between 4 October 2010 and 15 November 2010 near the 9 m isobath, approximately 130 m onshore of the KNO node, which included temperature observations (Seabird Electronics SBE 39) at depths of 8.7, 6.3, and 4.3 m relative to the mean water surface. Atmospheric data, including pressure, relative humidity, short wave radiation, and air temperature, were collected on the roof of the John A. Burns School of Medicine

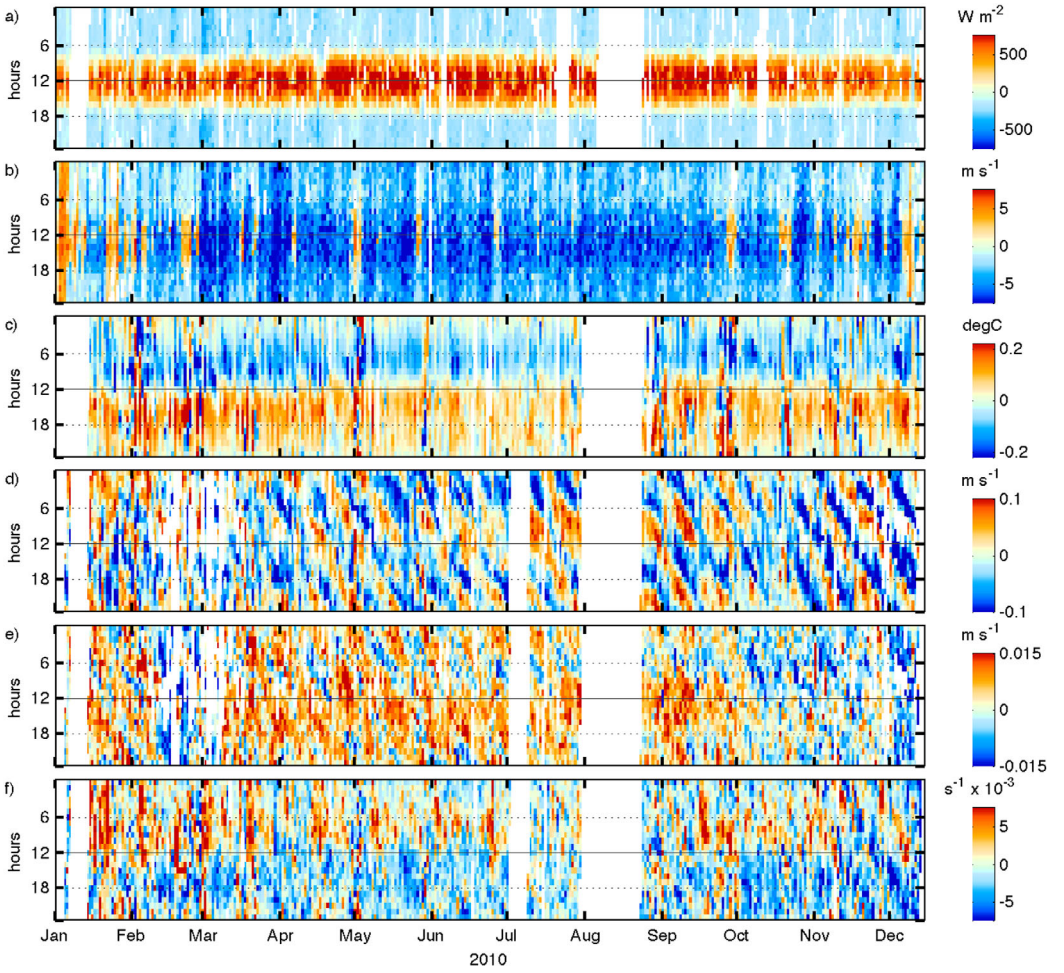


**Figure 3.** Summary of observations at KNO for 2010. The horizontal axis for all plots shows time of year and the vertical axis indicates time of day. (a) Surface heat flux, (b) cross-shore component of wind (positive onshore), (c) high-pass (33 h) filtered bottom water temperature, (d) depth-averaged alongshore water velocity (positive ESE), (e) depth-averaged cross-shore water velocity (positive onshore), (f) average middepth (3–10 m) cross-shore shear.

(JABSOM) located about 400 m inshore and 800 m from the KNO 12 m site. Wind speed and direction were acquired at hourly intervals from the Honolulu International Airport, about 7 km to the northwest.

The analysis presented here will make use of KNO data collected during 2010, focusing on the T-chain, ADCP, and meteorological data, as summarized in Figure 3. Each plot in the figure shows the diurnal variation (vertical axis) for a number of relevant variables over the full sampling period. The data time series have relatively good coverage for 2010, with a number of notable breaks; (1) the entire observatory was offline for most of August 2010; (2) T-chain data were unavailable in early January; (3) ADCP data were also interrupted in early January and in early July; (4) local atmospheric data were unavailable for short periods in late July and mid-October. As a quantitative measure, in total, at least 18 h of full data (T-chain, ADCP, wind, met-data) were available at the 12 m site on 249 days over the year.

Water velocity and temperature data were averaged into 20 min ensembles and meteorological data were averaged into 1 h ensembles to match wind observations. Data gaps less than 3 h in length were filled by linear interpolation to maximize coverage. Because the T-chain and the surface buoy thermistors were not jointly calibrated, there was an unknown offset between the two data sets. The offset was estimated by extrapolating the average stratification from the T-chain measurements, observed between midnight and 6 A.M., to the surface. We will revisit the choice of these hours later. Briefly, the stratification over the T-chain depths was observed to be weakest and to best follow a linear profile over these hours. The 9 m T-chain and the surface buoy sensors were both factory calibrated by Seabird Electronics and no offsets were applied to these data.

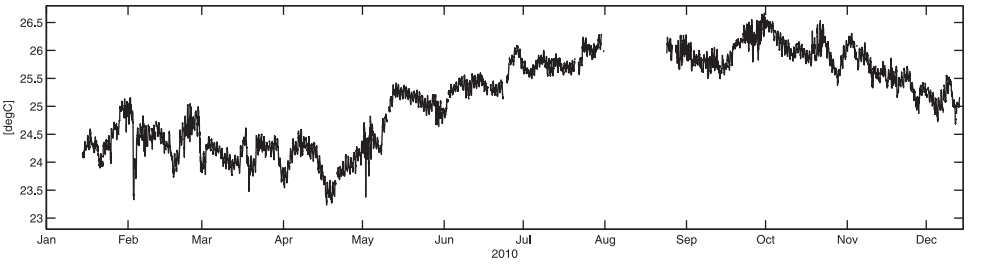


**Figure 4.** Time series of depth-averaged temperature at KNO for 2010.

The influence of salinity on density is neglected here because thermal contributions generally dominate density variations at KNO. In addition, observations of salinity at KNO show weak variations on diurnal time scales. Observations for salinity were available for part of the study period at the bed and surface. For the periods examined, changes in salinity were on the order of 0.01 psu, which translates to roughly an order of magnitude smaller change in density than the observed 0.2°C average diurnal changes in temperature. Vertical salinity stratification can play a role in the thermal structure at KNO, however, particularly during periods of increased rainfall. *Wells et al*. [2012] reported near-bed thermal inversions at KNO associated with radiative heating, which were compensated by weak vertical salinity gradients. These inversions were strongest during rainy periods.

Net surface heat flux, $\tilde{H}$, was calculated using the meteorological and SST data as the sum of shortwave, latent, sensible, and net longwave radiations [*Fung et al*., 1984; *Fairall et al*., 1996], where heating is positive and cooling is negative. Figure 3a shows the daily pattern in $\tilde{H}$ over the observation period, largely reflecting the seasonal changes in radiative heating. Nightly cooling, dominated by evaporation, is relatively steady throughout the year, consistent with very steady trade winds. The steadiness of the wind forcing is evident in the daily pattern in the cross-shore wind component shown in Figure 3b. The mean wind direction over the year was from the ENE (57°TN). The cross-shore direction here is defined as 27.5°TN (see Figure 2), based on the axis of minimum water velocity variance, where the axis of maximum variance captures the dominant alongshore tidally driven flow. Winds are then predominantly oriented offshore at KNO with an alongshore component in the negative $x$ direction (to the WNW). The cross-shore wind component shows a diurnal pattern, peaking in the early afternoon, but generally does not change sign. A few notable exceptions are associated with short bursts of onshore winds with the passage of low-pressure "Kona" storms which are most common during winter months [*Leopold*, 1948].

Figure 3c shows the high-pass filtered (33 h cutoff) water temperature at the bottom of the KNO T-chain for 2010, versus time of day. For reference, the annual variation in water temperature, shown for 2010 in Figure 4, shows a change of 2–3°C, with a minimum in March/April and a maximum in September/October [*Pawlak et al*., 2009]. The high-pass data show significant variability over time scales of multiple days, although a clear diurnal cycle is evident with a magnitude of $\pm$0.1°C, switching signs consistently near midday. Some of the high-frequency variability at KNO has been associated with shoaling internal waves (M. Squibb et al., manuscript in preparation, 2014) that are likely related to significant internal tides observed in Mamala Bay [*Eich et al*., 2004; *Alford et al*., 2006].

The depth-averaged alongshore velocity, shown in Figure 3d, has amplitudes on the order of 10 cm $s^{-1}$. A harmonic analysis of observations at KNO shows that the alongshore currents are predominately driven by the semidiurnal $M_2$ tide [*Pawlak et al*., 2009] as evident in the diagonal banding in the panel. There is considerable variability outside of the $M_2$ band notably evident in the first quarter of the year. Figure 3e shows the depth-averaged cross-shore velocity for the study period. The presence of persistent depth-averaged cross-shore flow is indicative of spatially variable two-dimensional (horizontal) circulation. Amplitudes are 1–2 cm $s^{-1}$ with a weak diurnal signal over most of the year, peaking in the onshore (positive $y$) direction the second half of the day. Very weak cross-shore tidal contributions are apparent as $M_2$ banding primarily evident during the early morning hours. For 2010, the time-averaged alongshore velocity was about 1.2 cm $s^{-1}$ to the WNW with a cross-shore average of about 0.3 cm $s^{-1}$ onshore. Maximum along and cross-shore velocities were 20–30 and 5–7 cm $s^{-1}$, respectively.

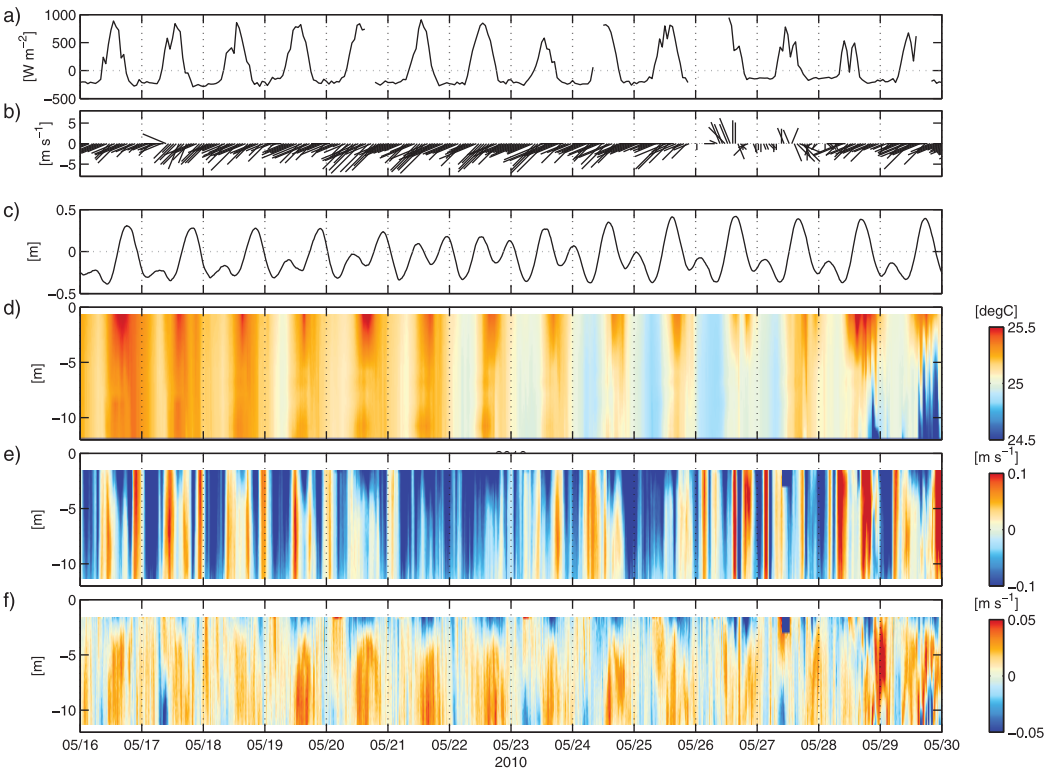


**Figure 5.** (a) Surface heat flux, (b) wind, (c) tidal height, (d) temperature, (e) alongshore velocity, and (f) cross-shore velocity at KNO for period showing a dominant thermal exchange regime.

Figure 3f shows the cross-shore middepth vertical shear, calculated as the average shear between 3 and 10 m depth. Positive shear indicates velocity decreasing with depth, for example, as associated with a onshore (positive) surface flow and an offshore (negative) flow near the bed. Of course, a unidirectional onshore flow would also give a positive middepth shear, so care must be taken in interpreting the shear as a measure of a thermally driven exchange. However, the diurnal pattern in middepth shear is opposite of that associated with the depth-averaged flow in Figure 3e, with positive shear during the first half of the day, changing signs roughly around midday.

While the diurnal structure is robust on an annual time scale, there is considerable variability in the flow structure at shorter time scales. A look at a sample 14 day period from late May (Figure 5) illustrates this variability. For the sample period, trade wind conditions are dominant apart from a 2 day period on 26–27 May. The temperature data (Figure 5d) highlight the diurnal cycle within a broader cooling trend. Vertical variation in temperature is typically weak during the morning hours, with surface intensified heating apparent in the afternoon. Weak thermal inversions are also evident over the second half of the day for some of the days in the time window, as reported earlier by *Wells et al*. [2012]. Although the dominant forcing frequency for both the alongshore flow and the surface tide over long time scales is the $M_2$, alongshore currents are notably decorrelated from the surface tidal height as observed by *Pawlak et al*. [2009]. For most of the period, the cross-shore flow shows an exchange flow structure that is consistent with the annual pattern seen in Figure 3, bracketed by periods where the diurnal structure is more chaotic. In particular, the diurnal structure appears to breakdown on 27 May following the change in wind regime and coincident with a reduction in surface heat flux. The thermal data also show a change in the diurnal pattern followed by a sharp increase in stratification. We will examine the relationship between the high variability in the exchange and the forcing mechanisms further in section 4.

The 2010 data in Figure 3 highlight the role of diurnal time scale processes, particularly in the cross-shore flow and is suggestive of a relation with diurnal thermal and/or wind stress forcing. The vertical structure of the diurnal flow averaged over the 2010 data set (Figure 6) reveals a robust pattern that is more consistent with thermally driven flow. The diurnal alongshore flow (Figures 6a and 6b) shows the influence of a

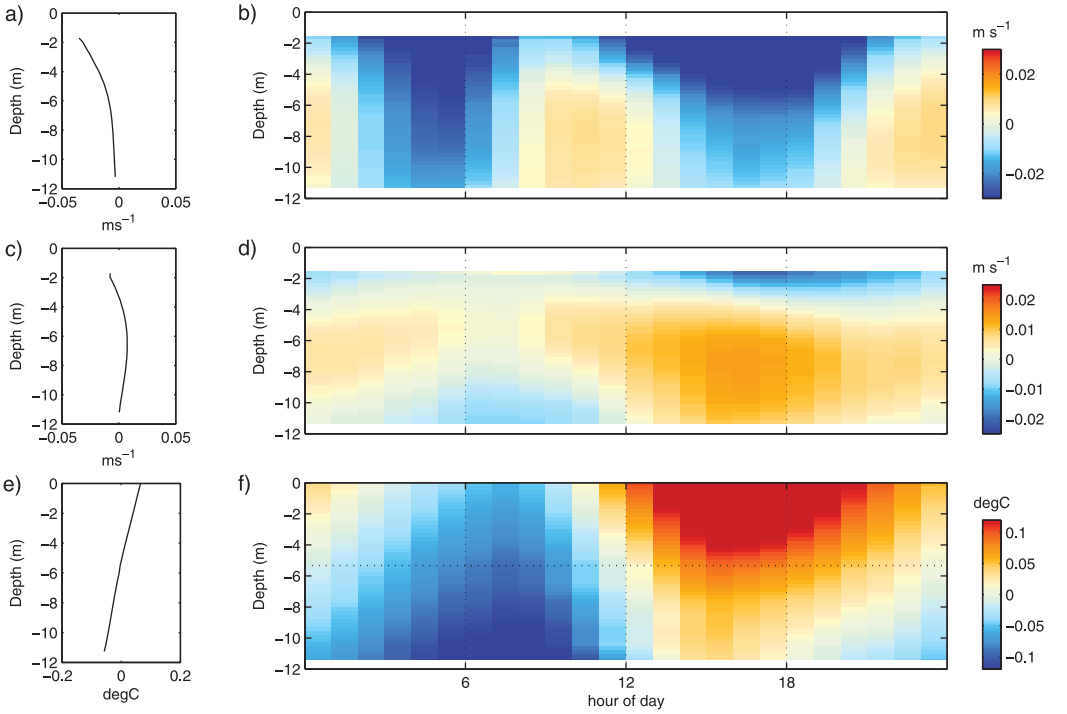


**Figure 6.** (a) Time-averaged alongshore velocity profile for 2010 data set versus depth and (b) variation in alongshore velocity (positive ESE) versus depth, time of day. (c and d) Same for cross-shore velocity. (e and f) Same for temperature (relative to annual average of 25.1°C).

semidiurnal ($S_2$) tidal component. The upper part of the water column shows a westward bias consistent with wind-driven flow. This westward component is dominant in the overall average profile (Figure 6a). The cross-shore velocity (Figures 6c and 6d) has a more distinctly baroclinic pattern, with offshore flow near the bed in the morning hours, changing direction in the afternoon/evening hours. The very near-surface flow is not well resolved by the ADCP due to sidelobe interference, but the flow at shallow depths appears to be generally offshore with stronger offshore flow over the second half of the day. The shear maximum in the cross-shore flow shifts from around 8 m depth in the morning to near 3 m in the afternoon, which results in the negative bias in the 3–10 m shear evident in Figure 3f. The overall cross-shore average profile (Figure 6c) shows an exchange with offshore surface flow and a return flow at depth. This time-averaged exchange can be accounted for in part as a result of the mean offshore wind stress but is also consistent with a time-averaged thermal exchange associated with a net gain of heat in the nearshore zone, discussed further below.

Water temperature (Figures 6e and 6f) reflects the diurnal heating/cooling cycle seen in Figure 3c with minimum values in the morning hours and a maximum in the mid afternoon. The combined temperature-velocity pattern is indicative of a thermally driven flow with cooler water advected offshore near the bed during the first half of the day and warm water flowing offshore near the surface during the second half of the diurnal cycle.

The temporal relationships between the diurnal flow and the forcing are more readily apparent in the average diurnal patterns shown in Figure 7. Here the surface heat flux is multiplied by the cross-shore distance $L_y = 400$ m so that it represents the total input over the region inshore of KNO, per unit alongshore distance. Both the depth-averaged temperature and the velocity shear are nearly 90° out of phase with the heat flux forcing. The cross-shore wind, in contrast, is persistently offshore, with a maximum amplitude in the mid afternoon.

The dominance of the diurnal response is evident in the spectral data in Figure 8. Temperature and cross-shore shear both respond primarily at a daily time scale with smaller peaks at semidiurnal frequencies corresponding to periods of 12 and 12.42 h. Spectra for the depth-averaged velocity components (Figure 8b) both have peaks at the $M_2$ frequency with notable peaks at its higher harmonics with the differing

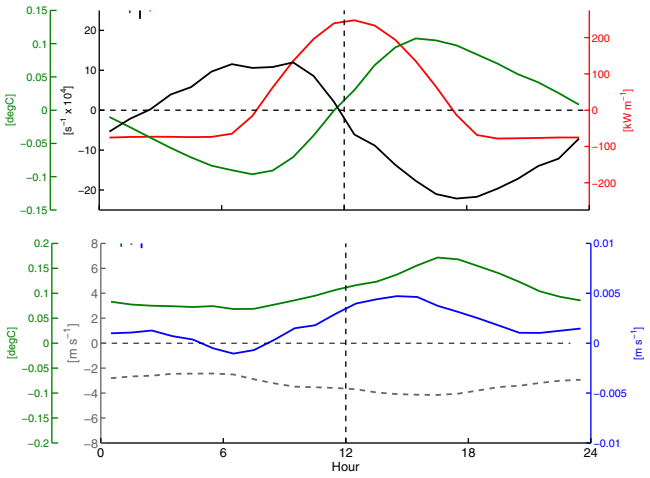


**Figure 7.** (a) Depth-averaged diurnal variations for 2010 for temperature (green), average (3–10 m) cross-shore shear (black), nearshore surface heat flux (red). (b) Top-bottom temperature difference (green), cross-shore wind (dashed gray), depth-averaged cross-shore velocity (blue). Vertical lines at top left in each plot indicate uncertainty in the mean (calculated as (standard deviation)/$\sqrt{n}$).

amplitudes reflecting the dominance of the alongshore flow. The cross-shore flow has a significant response at the diurnal time scale consistent with the pattern seen in Figure 3e.

## 4. Analysis

### 4.1. Relative Contribution of Exchange Flow

We can obtain a measure of the relative importance of the cross-shore exchange by comparing its contribution to the total cross-shore volume flux with that of the depth-averaged flow. We estimate the contribution due to the exchange for each 20 min interval for the 2010 data set as

$$\Gamma_{ex} = \frac{1}{2}\left\langle \int_{-D}^{0} |V(z) - \bar{V}| dz \right\rangle \quad (6)$$

where $\bar{V}$ is the depth-averaged velocity and $<>$ indicates low-pass filtering. The average time scale for nearshore flushing due to the exchange is then $\mathcal{V}/\bar{\Gamma}_{ex}$, where we use the time-averaged volume flux and $\mathcal{V}$ is the volume (per unit alongshore distance) of the nearshore region. The low-pass filter cutoff was chosen iteratively to be much smaller than the average flushing time scale, but long enough to eliminate short time scale fluctuations in volume flux that do not contribute significantly to nearshore flushing (as evident for the case of oscillations due to surface waves). The exchange volume flux estimated using equation (6) with a 3 h low-pass filter gives values that are comparable to the magnitude of the similarly defined depth-averaged cross-shore flux, as shown in Figure 9. For comparison, both mechanisms are generally greater than the 0.03 m$^2$ s$^{-1}$ volume flux necessary to flush an idealized 400 m $\times$ 12 m wedge in 1 day, approximating the region onshore of the measurement site. The average flushing time scales for the idealized wedge associated with the exchange and depth-averaged fluxes were 19.9 and 17.1 h, respectively. These values were not notably affected by changes in the low-pass cutoff. For 2010, $\Gamma_{ex}$ exceeds the depth-averaged flux 46% of the time.

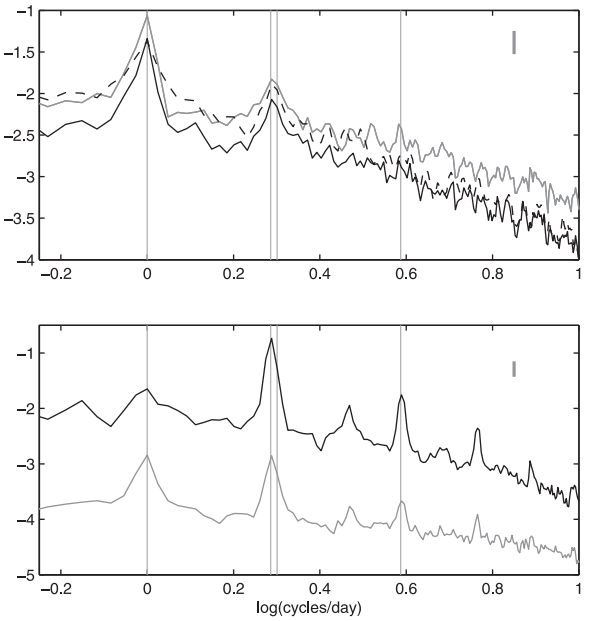


**Figure 8.** (a) Normalized autospectra for cross-shore shear (solid gray), top-bottom temperature difference (dashed gray) with shear-temperature cross-spectra (solid black). (b) Normalized autospectra for alongshore velocity (black), cross-shore velocity (gray). Velocity spectra are normalized by total velocity variance to highlight the relative values. In each plot, the vertical bar at top right indicates height of 95% confidence interval.

The contribution of the exchange is not cleanly captured in $\Gamma_{ex}$ since unidirectional flow will also have a sheared velocity profile. Attempts to remove the unidirectional component using an idealized logarithmic profile gave similar results, however, in part because the highest sheared region near the bed is not resolved

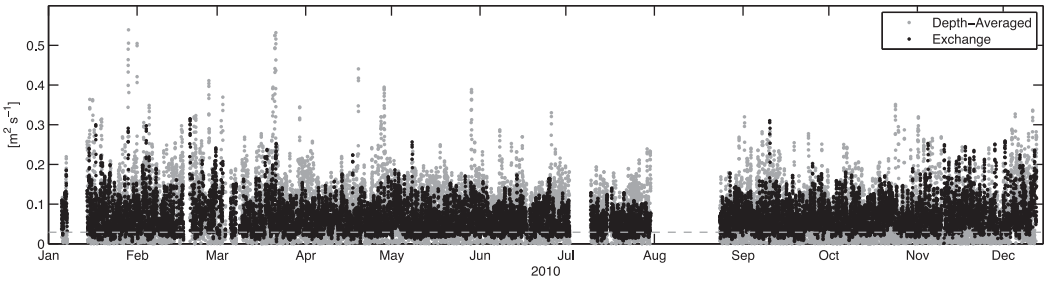


**Figure 9.** Approximate volume flux for KNO for 2010 due to depth-averaged flow (gray) and exchange (black). Horizontal dashed line indicates estimated flow rate required to flush nearshore region in 1 day.

by the ADCP observations. The observations thus indicate that the exchange portion of the cross-shore flow contributes significantly to nearshore flushing at KNO relative to the depth-averaged component.

### 4.2. Cross-Shore Exchange Momentum Balance

The phase relationships in the average diurnal structure (Figures 6 and 7) support the hypothesis that cross-shore exchange at KNO is driven primarily by surface heat fluxes. While the cross-shore component of the wind appears to influence the time-averaged flow structure, as evident in the average cross-shore velocity profile (Figure 6c) and in the asymmetry of the afternoon flow structure (Figure 6d), the phasing of the diurnal wind speed maximum (Figure 7b) is not reflected in the velocity shear, thermal response or cross-shore heat flux. In addition, the average diurnal pattern for the wind shows a persistent offshore flow that cannot account for the direction of the exchange in the first half of the day. An alternate hypothesis could be that the morning flow is a relaxation of a baroclinic structure induced by the offshore afternoon wind stress peak. This, however, would require cooler, upwelled water nearshore in the afternoon, with warming near the bed in the morning associated with the relaxation phase. This pattern is contrary to that observed. It is important to note, however, that, regardless of its effect in terms of a direct momentum flux, the wind plays a critical role in thermal exchange, via its effect on surface heat flux due to evaporation, particularly during the cooling phase.

The thermal response and the cross-shore shear (Figure 7a) both show a nearly 90° phase shift relative to the surface heat flux. Revisiting the discussion in section 2, the thermal response indicates a dominant unsteady flow regime in the context of equation (4). The ratio of the advective terms to the unsteady term, $\hat{V}\beta T_f/D$, will apply for both (1) and (4) so we might anticipate that an unsteady balance should also apply for momentum in (1). Recalling from section 2, an unsteady momentum balance implies that flow must be in quadrature with the cross-shore pressure gradient and in phase with the heat flux. The observations for the cross-shore flow at KNO show that the velocity response is *out* of phase (∼90°) with the forcing surface heat flux, however. If the advective term is negligible (relative to the unsteady term), this indicates that the turbulent diffusive term must play a dominant role and that a diffusive balance should apply at the KNO measurement site for both heating and cooling phases. This diffusive balance is consistent with the unsteady buoyancy balance where vertical mixing acts rapidly such that input of heat results in the observed temporal response in temperature over the full depth.

We can explore the roles of buoyancy and wind in the diurnal dynamic response in more detail by examining the various contributions to the cross-shore momentum balance. Averaging the cross-shore momentum equation (1) from the surface to $z = -z_L$ we obtain:

$$\frac{\partial \bar{V}_L}{\partial t} + \frac{\partial \overline{(V^2)}_L}{\partial y} - \frac{1}{z_L}(WV)_{-z_L} = -\frac{1}{\rho_0 z_L}\int_{-z_L}^{0}\frac{\partial P}{\partial y}dz + \frac{1}{z_L}\frac{\tau_w^y}{\rho_0} - \frac{1}{z_L}\left(\nu_t\frac{\partial V}{\partial z}\right)_{-z_L} - f\bar{U}_L \tag{7}$$

where the layer average is given by:

$$\overline{(\,)}_L = \frac{1}{z_L}\int_{-z_L}^{0}(\,)dz \tag{8}$$

Here we have assumed that variations in the sea surface elevation, $\eta$ are small relative to $z_L$. We have again assumed that the flow is well approximated as two dimensional and thus neglected the contribution from the correlation between the alongshore and cross-shore velocities. Equation (7) also neglects contributions due to wave forcing via radiation stress gradients and from the Hasselman wave stress [*Hasselmann*, 1970;

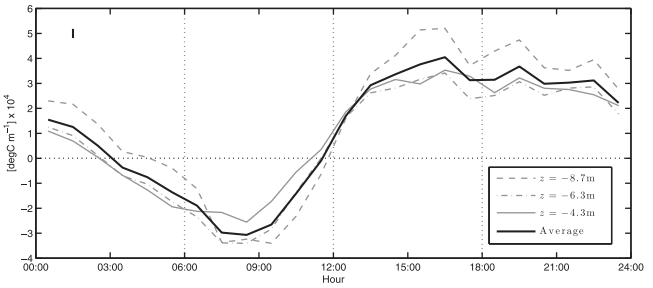


**Figure 10.** Diurnal variation in cross-shore thermal gradient for October/November 2010 time period, estimated between 9 and 12 m isobaths. Vertical bar at top left indicates estimated error magnitude for average gradient.

*Fewings and Lentz*, 2010]. We expect these to be relatively weak for the mild wave conditions at KNO. The cross-shore component of the wind stress is $\tau_w^y$. The third term on the LHS of equation (7) represents the vertical momentum transport due to turbulence at $z = -z_L$.

If we extend the average over the full water column ($z_L = D$), then we retrieve the depth-averaged cross-shore momentum equation:

$$\frac{\partial \bar{V}}{\partial t} + \frac{\partial \overline{V^2}}{\partial y} = -\frac{1}{\rho_0 D}\int_{-D}^{0} \frac{\partial P}{\partial y} dz + \frac{\tau_w^y}{\rho_0 D} - \frac{\tau_b^y}{\rho_0 D} - f\bar{U} \tag{9}$$

where $\tau_b^y$ is the cross-shore component of the bed stress. Subtracting the depth-averaged momentum (9) from (7) gives:

$$\begin{aligned}\frac{\partial}{\partial t}(\bar{V}_L - \bar{V}) + \frac{\partial}{\partial y}\left(\overline{(V^2)}_L - \overline{V^2}\right) - \frac{1}{z_L}(WV)_{-z_L} = &-\frac{1}{\rho_0 z_L}\int_{-z_L}^{0}\frac{\partial P}{\partial y}dz + \frac{1}{\rho_0 D}\int_{-D}^{0}\frac{\partial P}{\partial y}dz \\ &+ \frac{\tau_w^y}{\rho_0}\left(\frac{1}{z_L} - \frac{1}{D}\right) - \frac{1}{z_L}\left(\nu_t \frac{\partial V}{\partial z}\right)_{-z_L} + \frac{\tau_b^y}{\rho_0 D} - f(\bar{U}_L - \bar{U})\end{aligned} \tag{10}$$

which we can interpret as the momentum budget for the layer "exchange" velocity, $\bar{V}_{L_{ex}} = \bar{V}_L - \bar{V}$.

Making use of the hydrostatic equation, the pressure at depth $z$ is

$$p(z) = p_a + \rho_0 g(\eta - z) + g\int_z^{\eta} \rho' dz \tag{11}$$

where $p_a$ is the pressure at the surface. Here we have separated the density $\rho$ into the reference density $\rho_0$ and its spatially variable component $\rho'$. Using (11), the pressure gradient terms on the RHS in equation (10) then can be expressed as

$$-\frac{1}{\rho_0 z_L}\int_{-z_L}^{0}\frac{\partial P}{\partial y}dz + \frac{1}{\rho_0 D}\int_{-D}^{0}\frac{\partial P}{\partial y}dz = -\frac{g}{\rho_0}\int_{-z_L}^{0}\left(1 + \frac{z}{z_L}\right)\frac{\partial \rho'}{\partial y}dz + \frac{g}{\rho_0}\int_{-D}^{0}\left(1 + \frac{z}{D}\right)\frac{\partial \rho'}{\partial y}dz \tag{12}$$

In (12), we have considered that $\rho' \ll \rho_0$ and have again used the assumption that $\eta \ll D$ in neglecting additional terms associated with applying Leibniz's rule and in evaluating the integrals at $z = 0$. Assuming that density variations are associated with temperature, so that $\rho' = -\rho_0\alpha(T - T_0)$ then

$$\frac{\partial \rho'}{\partial y} = -\rho_0 \alpha \frac{\partial T}{\partial y} \tag{13}$$

The cross-shore thermal gradient between the 9 and 12 m isobaths was estimated at three depths (4.3, 6.3, and 8.7 m) for the October/November 2010 period during which the second thermistor chain was deployed. Figure 10 shows the diurnal variation in the thermal gradient for the three depths along with the average gradient. While the data suggest some depth variation in the gradient, particularly for the heating response, they indicate that an estimate of the pressure gradient can be obtained assuming a depth-independent thermal gradient. In that case, making use of (13), equation (12) simplifies to

$$-\frac{1}{\rho_0 z_L}\int_{-z_L}^{0}\frac{\partial P}{\partial y}dz + \frac{1}{\rho_0 D}\int_{-D}^{0}\frac{\partial P}{\partial y}dz = \frac{g\alpha}{2}(z_L - D)\frac{\partial T}{\partial y} \tag{14}$$

The net effect of the surface wind stress on the exchange momentum budget depends on the vertical flux of momentum due to turbulence which arises from the fourth term on the RHS of equation (10). The lack of water column turbulence observations preclude an accurate estimation of the turbulent flux, however. As discussed in section 2, the eddy viscosity will have contributions from turbulence associated with both

wind and bottom stress. The latter will be dominated by the much stronger alongshore flow. We can expect that stronger afternoon stratification (Figure 7b) may limit the turbulent flux to some extent, which could, in turn, confine the momentum input from the wind stress to the surface layer. The resulting stratification-driven acceleration of the near-surface flow by the wind has been previously observed by *Price et al*. [1986], who termed it the "diurnal jet." For the case where vertical flux is at a maximum, the contribution to the exchange will be minimal. In the other extreme, where turbulent flux is at a minimum, say due to very high stratification, the stress would contribute a maximum to the exchange momentum balance.

The advective contributions which appear in the second and third terms on the LHS of (10) are unresolved. We can draw some insight from the buoyancy budget, where the phase relation indicates that the unsteady term is dominant relative to the advective terms. As noted earlier, the ratio of the advective terms to the unsteady terms is the same in both (1) and (4). The dominance of the unsteady term relative to the advective terms in the buoyancy budget, discussed earlier, implies that the advective terms in (10) should also have negligible contributions.

Using (14), the exchange momentum budget in (10) can be written as

$$\frac{\partial}{\partial t}(\bar{V}_L-\bar{V})=\frac{g\alpha}{2}(z_L-D)\frac{\partial T}{\partial y}+\frac{\tau_w^y}{\rho_0}\left(\frac{1}{z_L}-\frac{1}{D}\right)+\frac{\tau_b^y}{\rho_0 D}-f(\bar{U}_L-\bar{U})+R \tag{15}$$

The residual $R$ in (15) then includes contributions due to the advective terms in (10) along with the unresolved vertical turbulent flux and any fluxes associated with deviations from two-dimensional flow.

The surface wind stress was estimated using a constant surface drag coefficient of 1.1 $(10)^{-3}$ and using the measured wind velocities. The cross-shore bottom stress was estimated as $\tau_b^y/\rho_0=C_D\bar{V}_{L_B}|\vec{U}_{L_B}|$, where $\bar{V}_{L_B}$ is the bottom layer cross-shore velocity and $\vec{U}_{L_B}$ is total bottom layer velocity vector. The velocities $\bar{V}_{L_B}$ and $\vec{U}_{L_B}$ are averaged over $-z_L<z<-D$. A relatively high drag coefficient of $C_D=0.015$, consistent with the very high reef roughness, was used, based on previous measurements at KNO [*Jones et al*., 2008; A. G. Collignon et al., manuscript in preparation, 2014]. The drag will increase during periods of higher wave forcing [*Grant and Madsen*, 1979; Collignon et al., manuscript in preparation], but the value chosen is representative of typical, low-wave conditions.

Velocities for the surface and bottom layer for the October/November time period averaged by time of day, are shown in Figure 11a, where the layer depths are chosen as 0–4 and 4–12 m, respectively. The "exchange" velocity $V_{L_{ex}}$, as defined above, is shown for both layers. The full year average exchange components, also shown in Figure 11a, illustrate that the exchange during the October/November subset, while slightly stronger, is representative of the full data set. The layer depths were chosen to highlight the heating response phase, where the cross-shore velocity zero crossing is approximately at 4 m (Figure 6), in order to examine the relative contributions of wind stress and baroclinic forcing for this phase. The 4 m layer depth is less appropriate for the cooling phase response where the surface layer is much thicker. This is evident in the weaker layer velocities during the morning hours in Figure 11a. For these times, the onshore cooling phase surface flow has a maximum centered at roughly 6 m, with the zero crossing at about 8–10 m, so that its contribution is averaged into the lower layer.

In Figure 11b, we examine dominant contributions to the diurnal cross-shore "exchange" momentum budget in equation 15 for the surface (0–4 m) layer. Time series for each term are calculated and values are then averaged by time of day to examine diurnal variations. The principal contributions are from the baroclinic pressure gradient (RHS term 1, equation (15)) and the wind stress (RHS term 2, equation (15)). The wind stress input is shown both for the Oct/Nov subset and for the annual average, again indicating that the subset period provides an adequate representation of average conditions. The diurnal pattern for wind stress has a steady offshore component with a peak in the afternoon. The baroclinic pressure gradient changes direction following the thermal gradient, consistent with the general exchange pattern in Figure 6d. The dominant momentum terms indicate that, in the limit of zero vertical momentum flux, the wind stress contribution to the exchange momentum can be comparable to the baroclinic term for KNO.

The unsteady term (LHS term 1, equation (15)) is small over the diurnal cycle. Based on the buoyancy response, the neglected advective terms should be comparable or smaller, further supporting their exclusion in the analysis. The contribution of the bottom stress (RHS term 3, equation (15)) to the exchange

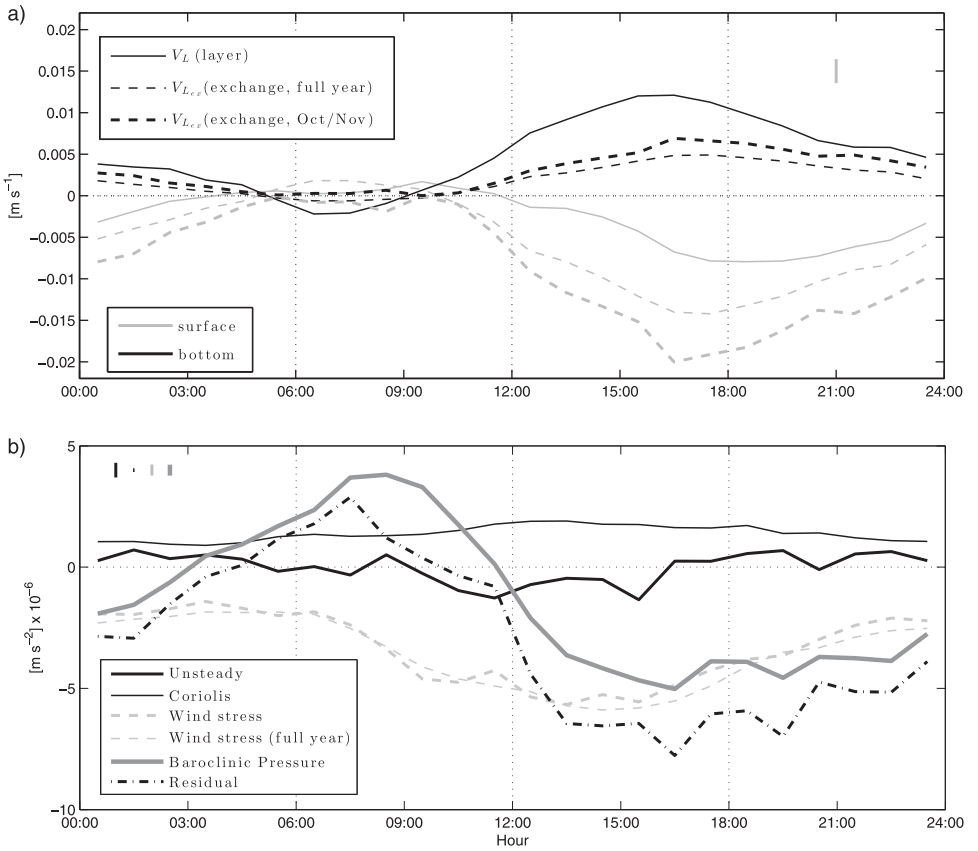


**Figure 11.** (a) Cross-shore layer-averaged and exchange velocities for surface (0–4 m) and bottom (4–12 m) layers. (b) Cross-shore momentum budget terms for the surface layer for the October/November 2010 subset. Wind stress term for full year is also shown for comparison. Vertical bars at top left indicate estimated error magnitudes. Errors in velocities in Figure 11a are similar for all quantities. For Figure11b, wind stress error (not shown) is nearly identical to that for baroclinic term.

momentum is generally comparable to or smaller than the unsteady contribution so this is not shown. The Coriolis term (RHS term 4, equation (15)) contributes an onshore component to the surface exchange budget, associated with the mean westward flow (Figures 6a and 6b). On any particular day, however, its contribution may be more substantial, given stronger variable alongshore tidal currents.

The residual associated with the unresolved terms in equation (15) is substantial. The remaining unresolved contribution is likely attributable to vertical turbulent fluxes (again limited by the assumption of 2-D flow with weak advective components). This result is consistent with the earlier observation that the phasing of the cross-shore shear requires a dominant diffusive momentum balance. Furthermore, the diurnal variation in the residual is also generally consistent with the vertical shear indicated by the layer velocities in Figure 11a and that shown in Figure 7a. Notably, the required high vertical turbulent transport would also suggest that the net contribution of the wind stress to the exchange is likely overestimated by using the maximum value as we have done here.

### 4.3. Thermal Balance

Figure 12 compares the unsteady term in equation (4), $\partial B/\partial t = -\alpha g \partial T/\partial t$ to the forcing term expressed as the surface heat flux distributed over the depth, $\partial \tilde{F}/\partial z = -\alpha g \tilde{H}/\rho_0 C_p D$. It is apparent from the residual that the unsteady balance is largely applicable at the 12 m isobath over the course of the day, as suggested by the phase relationships. The slight phase lead in the thermal response along with the corresponding negative residual in the afternoon indicates that advective fluxes play a role in removing heat later in the day.

The average heat input during the daytime heating phase (between 800 and 1700) totals about 1.4(10)$^4$ kJ m$^{-2}$ at the KNO 12 m site or 5.43(10)$^6$ kJ per alongshore meter (from integrating the heat flux in Figure 7a

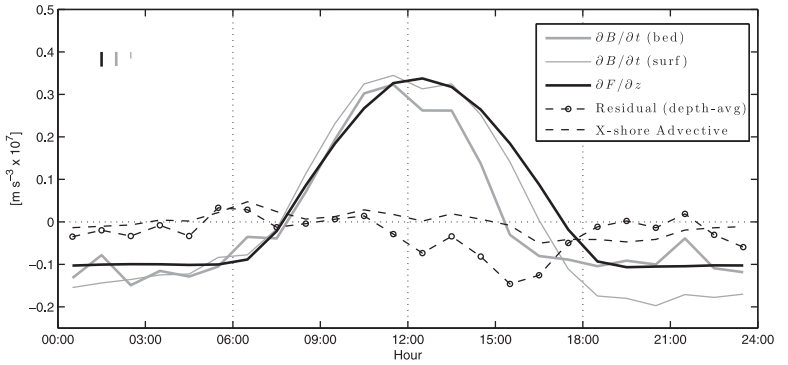


**Figure 12.** Diurnal variation in temporal rate of change for buoyancy, near bed: solid gray, near surface: dashed gray and surface heat flux forcing (solid black). Vertical bars at top left indicate estimated error magnitudes.

over heating hours) for the region inshore of the measurement site. The change in local depth-averaged temperature (Figure 7a) over the heating phase accounts for roughly 77% of heat input at the 12 m isobath. If we extend this fraction across the entire inshore region, the remaining 23% of the heat input or $1.24(10)^6$ kJ m$^{-1}$ must be accounted for via advective transport. Advective transport can be associated either with the cross-shore exchange, the depth-averaged cross-shore flow or with lateral (alongshore) divergence.

The total cross-shore advective heat transport per unit alongshore distance is given by:

$$Q_{tot}(\tau)=\rho c_p\int_{-D}^{0}\langle V(z)T(z)\rangle_\tau dz \tag{16}$$

where $\langle\,\rangle_\tau$ indicates ensemble averaging by time of day, $\tau$. This is an impractical formulation, however, since it describes the absolute heat transport, which is a large quantity, balanced by a similarly large quantity associated with the unresolved alongshore flux. If we instead separate the temperature into a depth-averaged low-frequency component and a depth-variable "high-pass" component, so that $T(z)=T_{HP}(z)+\bar{T}_{LP}$, we can examine contributions due to short time scale variations. The contribution from the low-pass temperature retains the large quantity (mostly balanced by the alongshore flux), while the high-pass contribution in equation (16) will be a much smaller value. Since we are interested in the diurnal time scale variations, we will focus on the variations associated with $T_{HP}(z)$. This component is then given by:

$$Q_{xs}(\tau)=\rho c_p\int_{-D}^{0}\langle V(z)(T(z)-\bar{T}_{LP})\rangle_\tau dz \tag{17}$$

Note that this is not precisely a high-frequency component, since the depth variable portion can include a low-frequency variation. In addition, the cross-shore velocity $V(z)$ can also include low-frequency variations.

Variations in the low-frequency temperature will result from small diurnal imbalances, although for an "average" day (averaged over a full year), the change in $\bar{T}_{LP}$ over a full day should be negligible relative to the surface heat flux and the advective contributions. The low-frequency cross-shore component associated with $\bar{T}_{LP}$ can, of course, contribute to the diurnal heat budget although this is not determined here since we do not resolve the alongshore heat flux.

We can isolate the cross-shore heat flux associated with the average diurnal exchange flow as

$$Q_{ex}(\tau)=\rho c_p\int_{-D}^{0}\langle(V(z)-\bar{V})(T(z)-\bar{T}_{LP})\rangle_\tau dz \tag{18}$$

where $\bar{V}$ is the depth-averaged cross-shore velocity. Note that the definitions for both $Q_{ex}$ and $Q_{xs}$ implicitly include fluxes associated with fluctuations in velocity and temperature that occur at time scales greater than the 20 min averaging time. These "Reynolds" fluxes are analogous to turbulent fluxes, although the mechanisms may not be associated with turbulent processes. The cross-shore advective contribution to the high-frequency flux associated with the depth-averaged flow can be estimated from the difference as $Q_{da} = Q_{xs} - Q_{ex}$.

Diurnal variations for cross-shore advective heat transport for the exchange and depth-averaged components are shown in Figure 13 as estimated from the data, with $\bar{T}_{LP}$ based on a 66 h cutoff. Because velocities very near the surface and the bed are lacking, transport in the near-surface region is estimated using the

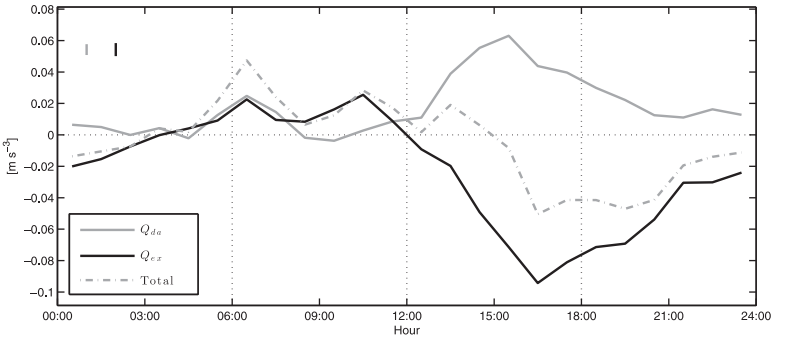


**Figure 13.** Advective contributions to cross-shore heat flux from depth-averaged ($Q_{da}$, gray) and exchange flow ($Q_{ex}$, black) components. Net cross-shore advective flux is shown by the dashed gray line. Vertical bars at top left indicate estimated error magnitude for depth-averaged (gray) and exchange (black) fluxes.

top-most velocity bin (∼1.75 m depth) with the near-bed transport calculated using half of the lowest velocity measurement (∼0.8 m above the bed).

The diurnal profile for $Q_{ex}$ (Figure 13) shows a weak positive flux during morning hours with a stronger negative flux during the afternoon. The negative bias indicates a net heat loss for the nearshore region. The contributions to $Q_{ex}$ can loosely be interpreted via the diurnal variations in shear (Figure 7a) and the top to bottom temperature difference (Figure 7b). The stronger vertical temperature difference in the afternoon contributes to the average negative heat flux. The time-averaged profiles shown in Figures 6c and 6e also contribute to a net seaward thermal flux.

We can consider the contributions associated with Reynolds fluxes if we define advective fluxes using the product of the velocity and temperature averages rather than the average of the products as in (18). Advective fluxes estimated in this manner are not notably different from those shown in Figure 13, for both the depth-averaged and exchange components, however. This indicates that the contributions due to Reynolds fluxes for time scales longer than the 20 min averaging period are not significant. Analysis using the higher sampling frequency raw ADCP and T-chain data indicates that contributions from Reynolds fluxes at shorter time scales are an order of magnitude smaller than the fluxes plotted in Figure 13 so these are not included in our discussion.

Integrated surface and advective heat flux contributions to the nearshore heat budget over selected diurnal periods are summarized in Table 1. Uncertainties are calculated based on the integrated errors in surface heat flux and in the advective fluxes, which are shown by the vertical bars in Figures 7a and 13. Because the cross-shore exchange heat flux ($Q_{ex}$) is roughly in quadrature with the surface heat flux, its contribution to the heat budget over the heating phase accounts for an export of only about 20% of the required advective transport (about 5% of the incoming surface heat flux). This advection is nearly offset by the depth-averaged cross-shore contribution $Q_{da}$, however, which provides an *input* of heat to the nearshore zone equivalent to about 23% of the necessary advective flux over heating hours. Although the fraction of surface heat flux that goes toward changes in temperature can be expected to vary in the cross-shore direction relative to the 77% value at the 12 m isobath, these observations indicate that a heat loss due to the unresolved low-frequency component and an alongshore divergence must provide a significant contribution to the local thermal budget.

As the heating phase progresses, heat accumulates inshore establishing the cross-shore pressure gradient that drives the cross-shore exchange. Toward the end of the heating phase, the resulting advection begins to contribute to the thermal balance and, combined with the increasing contribution associated with the depth-averaged flow, drives a reduction in local temperature prior to the end of the heating. This appears as a small phase shift in the peak temperature relative to the surface heat flux zero-crossing evident in

**Table 1.** Integrated Diurnal Surface and Advective Heat Fluxes

| | Cooling 1700–800 | Heating 800–1700 | Cooling Response (kJ m−1 × 105) 0000–1200 | Heating Response 1200–0000 | Full Day |
|---|---|---|---|---|---|
| Surface heat flux | −35.6 ± 0.8 | 54.3 ± 1.4 | – | – | 18.7 ± 2.2 |
| Exchange | −4.7 ± 1.6 | −2.5 ± 1.1 | 0.8 ± 1.2 | −8.0 ± 1.4 | −7.2 ± 2.2 |
| Depth averaged | 2.8 ± 1.3 | 2.9 ± 0.9 | 0.9 ± 1.1 | 4.7 ± 1.1 | 5.7 ± 2.6 |
| Total cross shore | −2.0 ± 2.1 | 0.4 ± 1.4 | 1.8 ± 1.7 | −3.3 ± 1.8 | −1.5 ± 3.5 |

Figure 7a. If we apply the advective flux measured at the 12 m isobath across the nearshore zone and assume a wedge profile, we can compare the contribution of the high-frequency net flux in Figure 13 to the buoyancy terms. Figure 12 includes the high-frequency advective flux in terms of a bouyancy flux, $\alpha g Q_{xs}/(\rho C_p L_y D/2)$. Note that the terms plotted in the figure are calculated only at the 12 m isobath, so the comparison is not precise, but it allows us to illustrate the role of advection in the buoyancy budget.

Although the exchange contribution is small during the daytime hours, over the course of the heating response phase (1200–0000) the cross-shore exchange transport is more substantial, exporting an estimated 65% of the advective flux.

The average local heat loss during the nightly cooling phase (1700–900) is $8.9(10)^3$ kJ m$^{-2}$ at the 12 m site or $3.56(10)^6$ kJ m$^{-1}$ applying the 12 m value across the nearshore region. This is mostly balanced by the heat loss associated with the peak to peak decrease in local temperature as suggested by the unsteady balance shown in Figure 12. The drop in local temperature exceeds the surface flux, however, (about 117%) again reflecting the importance of the various advective modes which must provide the additional heat loss. The exchange contribution over the cooling hours roughly accounts for the thermal imbalance with an export of 13% of the surface heat loss. The depth-averaged flow, however, contributes a *gain* of estimated 8% which again points toward a matching heat loss due to alongshore divergence.

Overall, for the data considered here, the integrated surface heat flux results in a gain of $1.87(10)^6$ kJ m$^{-1}$ per day for the inshore region, which must be removed by advection. The high-frequency depth-averaged flow contributes an additional input of 30% of the daily surface heat input. Over the course of the day, the average cross-shore exchange exports roughly 38% of the integrated surface heat flux. The net offshore thermal advection by the exchange flow is evident from the time-averaged profiles in Figures 6c and 6e. So, while the role of the thermal exchange in the thermal balance is relatively small over the heating/cooling time scales due to its phasing, its net contribution in removing heat on diurnal time scales is significant. The net surface input of heat and the resulting seaward advective flux can account, to some extent, for the relatively weaker cooling response in the thermal exchange apparent in the shear and heat flux diurnal patterns.

Together, the cross-shore contributions still leave an excess of heat of about $1.7(10)^6$ kJ m$^{-1}$, or 92% of the integrated surface input, that must be accounted for by the unresolved low-frequency component and the alongshore thermal divergence. The importance of alongshore divergence was suggested by the net onshore volume flux described earlier, along with the dependence of the cross-shore exchange on the alongshore flow direction (Figure 14d). These two observations point toward the existence of alongshore gradients in velocity and temperature that can help account for the observed imbalance in the heat budget.

Although the errors associated with the diurnal averages are small when estimated over the year-long data set, the variability in these patterns is significant, as evident in Figures 3 and 14. Nevertheless, the thermal budget highlights the importance of the exchange in the advective heat transport on a diurnal time scale.

### 4.4. Variability in Cross-Shore Exchange

While the averages shown in Figures 6 and 7 are characterized by significant velocity magnitudes (cross-shore exchange velocities that are ~10–20% of typical alongshore velocities), the time series data in Figures 3 and 9 indicate that cross-shore flow structure is subject to high temporal variability. The snapshot in Figure 5 suggests a relationship to winds and/or to surface heat flux as might be anticipated from the cross-shore momentum budget and from the influence of the wind via evaporation. The importance of turbulent fluxes along with the Coriolis contribution in the exchange momentum balance both indicate that variability in the alongshore flow may also play an important role.

In order to examine the effects of the various mechanisms on the magnitude and structure of the cross-shore exchange, ensemble diurnal averages were calculated based on forcing characteristics defined for each measurement day. Figure 14 shows the variation of cross-shore exchange in terms of three key measures as a function of various possible forcing variables. The exchange was measured using average vertical shear, $\delta V_z$ (between 3 and 10 m), top-bottom temperature difference $\Delta T_z$, and vertically averaged high-frequency cross-shore advective heat flux $Q_{ex}$ (as defined in equation (18)). For example, Figure 14a/Figure 14b illustrates the effects of daily surface heating/cooling fluxes on these three quantities. Heating/cooling flux values were assigned for each day based on averages over the corresponding heating/cooling time periods (800–1700 for heating, 1700–800 for cooling). Measures of $\delta V_z$, $\Delta T_z$, and $Q_{ex}$ were then averaged by

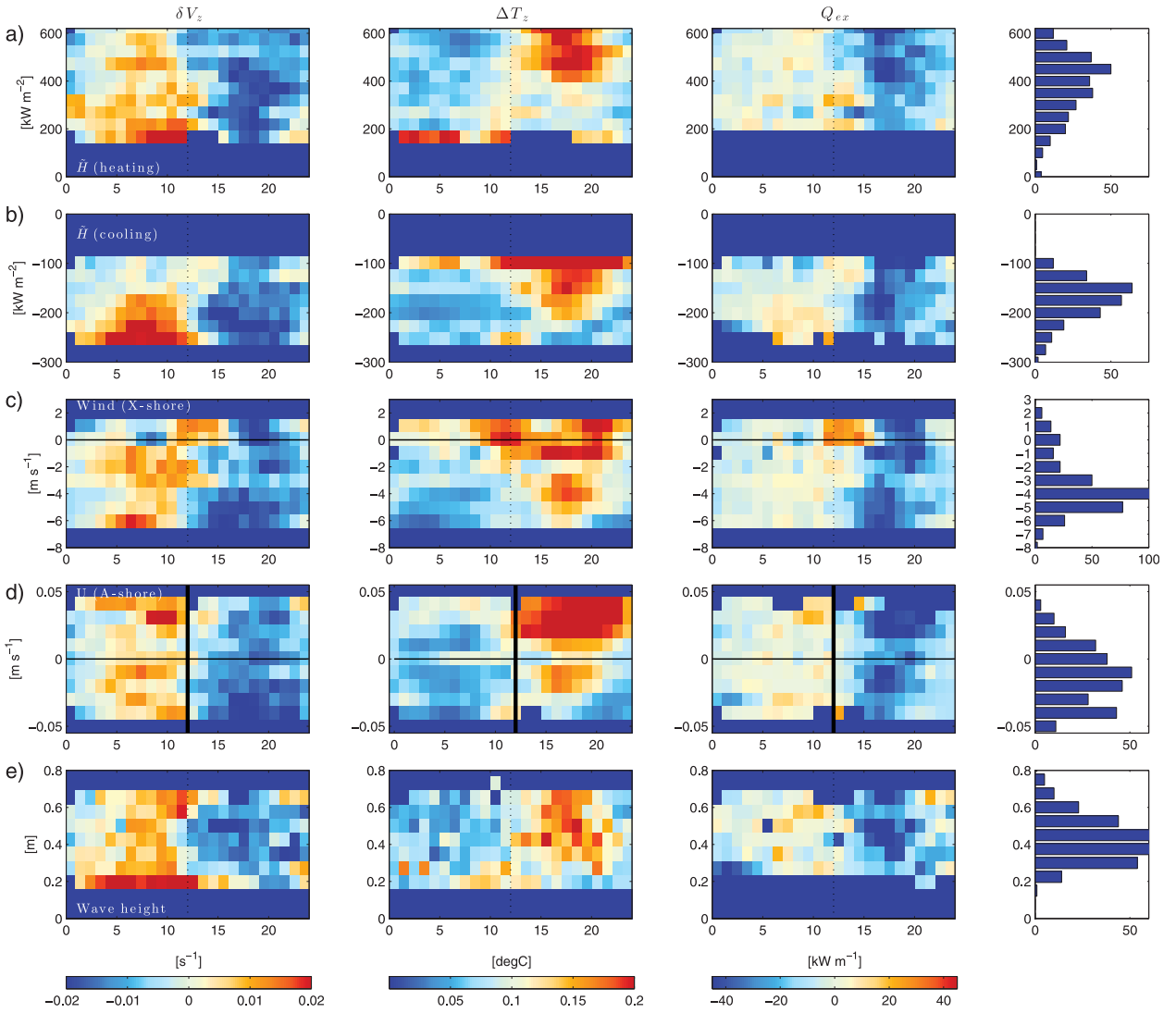


**Figure 14.** Ensemble-averaged diurnal profiles for (column 1) vertical shear ($\delta V_z$, 3–10 m depth), (column 2) top-bottom temperature difference ($\Delta T_z$), (column 3) cross-shore exchange heat flux ($Q_{ex}$) versus daily averaged: (a) heating (800–1700), (b) cooling (1700–800), (c) cross-shore wind magnitude (full day), (d) alongshore current velocity (0000–1200, 1200–000 for night/day profiles, respectively), (e) significant wave height (full day). Histograms with number of days contributing to each ensemble (column 4).

time of day over days with average daily surface heating/cooling fluxes within similar bands (50 W m$^{-2}$). Figures 14c–14e examine the variation of the exchange as a function of cross-shore wind, alongshore velocity and wave height, respectively.

As daily averaged heat input increases (Figure 14a), the shear weakens slightly in magnitude during the heating response phase (1200–2400), but broadens in time. There is a marked increase in $\Delta T_z$ with increasing heat input during the heating response with an associated increase in cross-shore heat flux. For increased cooling (Figure 14b), cooling phase $\delta V_z$ increases notably, driving increased $Q_{ex}$. Interestingly, heating phase $\delta V_z$ also increases for increased cooling, although this is offset by a decrease in $\Delta T_z$. The effects of wind (Figure 14c) are fairly uniform for offshore (negative) directed wind, but an increase in shear along with a slight shift in phase toward earlier afternoon is evident for strong winds. Significant changes are observed for onshore or low winds, however. Here the typical diurnal structure apparent in the averages appears to break down, with strong heating dominating daylight hours. In general, low winds coincide with weak cooling due to the reduction in evaporation and the patterns associated with these limits are similar.

Average alongshore velocity (Figure 14d) has a significant influence on the cross-shore structure, most notably on $\Delta T_z$. Heating is markedly higher for positive (ESE) currents. Recalling the discussion associated with

the thermal balance, the asymmetry in $\Delta T_z$ is indicative of an alongshore gradient in temperature, which would contribute to a heat flux via an alongshore divergence.

We might anticipate stronger exchange for positive alongshore velocity due to the influence of the Coriolis term in equation (10). The opposite is observed, however, likely because strong westward flow (negative alongshore) is also associated with strong northeasterly trade winds, which augment the exchange. Despite the increase in exchange shear for negative currents, the net effect is an increase in $Q_{ex}$ for positive alongshore flow. Finally, variations in exchange variables due to changes in wave forcing (Figure 14e) do not show clear patterns, likely due to the small range of wave conditions, although there is an indication that shear and cooling weaken for stronger waves.

## 5. Discussion

The observations described here indicate that the exchange portion of the cross-shore flow contributes significantly to nearshore flushing and to the thermal balance at KNO relative to large-scale patterns in depth-averaged horizontal flow. Analysis of the momentum balance indicates that the cross-shore thermal gradient provides the dominant forcing mechanism although surface wind stress also plays an important role. Ensemble averages in Figure 14 further support the conclusion that cross-shore flow structure is driven by surface heat fluxes, modulated by wind and alongshore flow direction. The observations illustrate the complexity of the cross-shore flow and indicate that alongshore variability has important implications for the exchange. For the KNO site, we can speculate that the thermal variations are associated with localized heating/cooling over the shallow reef flat located onshore and to the NW of the measurement site.

Despite the high variability of the exchange, the observations show that the phase relationships are robust over the 2010 measurement period. The phasing of the thermal response relative to the surface heat flux at all depths (Figures 6e and 6f) indicates that the unsteady term is dominant relative to the advective inertia term in the buoyancy equation. Comparison of the unsteady term in equation (4) to the forcing term (Figure 12) confirms that the buoyancy balance is predominantly in the unsteady regime. The phasing for the momentum response is not consistent with the unsteady regime, however, indicating a diffusive balance.

The observed cross-shore thermal gradient (Figure 10) is in quadrature with the surface heat flux, again consistent with an unsteady buoyancy regime. Examination of the exchange momentum balance indicates that the associated baroclinic pressure gradient is more than sufficient to drive the observed exchange velocities. The baroclinic gradient is augmented by wind stress during the afternoon and opposed during the morning cooling response. A significant imbalance in the exchange momentum remains, particularly during the afternoon, that is, likely accounted for by a vertical turbulent diffusive flux. Although measurements of the turbulent fluxes were not available, the observed residual is consistent with the phase of the vertical shear.

The dominantly cross-shore wind stress at KNO complicates the interpretation of the cross-shore flow response. The contribution of the surface wind stress to the exchange momentum budget cannot be firmly established in the absence of turbulence measurements, but two limiting cases have been considered. If the wind stress is distributed uniformly in the vertical by turbulent fluxes, then its contribution to the exchange will be small, since the stress will contribute instead to the depth-averaged flow. If the vertical extent of the wind stress is confined by stratification (the diurnal jet response) then the contribution of the wind to the exchange is maximal. The latter case was considered in the momentum balance, although the conclusion that a significant vertical diffusive flux is required to close the budget suggests that the actual case is likely closer to the former. The phasing of the depth-averaged flow is, in fact, well correlated with the wind, although in the opposite sense from that expected from the local stress. This implies the presence of barotropic gradients associated with wind-driven setup at larger scales. Between direct effects of wind stress, contribution to heat flux via evaporation and 2-D flow resulting from spatial wind stress gradients, wind effects play a nonnegligible role in the cross-shore flow at KNO as evident in the ensemble averages in Figure 14.

*Cormack et al.* [1975] found that a relatively small surface wind stress could have fairly significant impacts on the flow response for buoyancy-driven flow in a shallow rectangular cavity. For the wedge case, *Farrow* [2013] examined the effects of periodic wind stress on thermally forced flow using a linear analytical model.

A favorable wind stress, in phase with the thermally driven flow led to increased transport with little change in flow structure. For the case where the wind stress opposed the thermal forcing, the flow response varied with cross-shore distance with buoyancy forcing dominant close to shore transitioning to wind stress dominated flow offshore. At KNO, the prevailing offshore trade winds reinforce the heating response phase, but oppose the cooling response. This may account, to some extent, for the observed asymmetry in the exchange (i.e., Figure 13). The analysis by *Farrow* [2013] also suggests zones of surface divergence during the cooling phase where nearshore shoreward flow transitions to offshore wind-driven flow.

The source of turbulence that drives the vertical diffusion of heat and momentum can have multiple sources as noted earlier. Both cross- and alongshore components of the wind can introduce shear that can drive vertical fluxes. The low velocities associated with the cross-shore flow are unlikely to provide a substantial source for turbulence via shear or bottom stress. The stronger alongshore tidal flow, with an average velocity magnitude of $\sim$5 cm $s^{-1}$, provides a much more likely source. We can estimate the associated vertical momentum flux using an eddy viscosity argument with $v_t = \kappa u^* h$, where $u^* = 6(10)^{-3}$ m $s^{-1}$ is the bed stress associated with the typical alongshore flow (using $C_D = 0.015$) and $h$ is the height above the bottom. The turbulent flux term in equation (10), evaluated at middepth for simplicity (so that $z_L = h$), can then be estimated as $\kappa u_* |\partial V/\partial z|_{-z_L}$ Using a representative shear magnitude of $|\partial V/\partial z| \approx 0.02$ $s^{-1}$ for the heating phase (Figure 7a) gives a flux of $5(10)^{-6}$ m $s^{-2}$, comparable to that associated with the wind stress and with the residual in the momentum balance (Figure 11b). Vertical fluxes due to the alongshore flow, combined with contributions associated with wind stress, can thus readily account for the residual in the momentum budget. Ensemble averages of the exchange variables as a function of estimated bed stress and velocity magnitude (not shown here) were inconclusive in identifying a relation, however, possibly due to the dominant influence of the velocity direction, as seen in Figure 14.

For the nightly cooling phase, vertical convection would also contribute to vertical diffusive transport. *Sevadjian et al*. [2010] observed mixing of thin zooplankton layers along with a breakdown in stratification at KNO at diurnal time scales, attributed to nightly cooling. Observations of the vertical temperature difference (Figure 7b) for 2010 show diminished thermal stratification consistent with additional convectively driven vertical mixing. Thermal stratification is at a minimum between 0000 and 600, justifying the use of these hours in the temperature cross calibration between the T-chain and the surface buoy thermistor, described in section 3.

As evident in Figure 13, the contributions due to nondiurnal correlations in temperature and velocity ("Reynolds" fluxes) are small in the diurnal advective fluxes. These fluxes can be associated with larger-scale instabilities in alongshore currents, or in wind and wave-generated flow patterns. We can anticipate, then, that these fluxes may be more important for individual daily balances and over shorter time scales, where these mechanisms might align constructively or destructively with the diurnal forcing. These nonlinear relations can also be expected to contribute to the high variability observed in the cross-shore flow, but are not well represented in the diurnal ensembles presented in Figure 14.

The variability in the cross-shore flow with alongshore flow direction indicated by the ensemble averages in Figure 14d, along with the contribution of alongshore divergence in the heat budget, suggests a more complex three-dimensional structure for the thermally driven flow that may limit the applicability of the 2-D structure formulated in the theory in section 2. This variability is likely associated with alongshore variations in bathymetry that result in gradients in temperature as well as in turbulent transport. Given the observed velocity magnitudes and direction, the higher temperature changes observed for positive (ESE) flow at KNO are likely associated with increased heating/cooling on the shallow reef flat located to the NW of the observation site (Figure 2). Spatial variability can also be introduced by alongshore variations in wind stress. Measurements at other alongshore locations can thus be expected to similarly reflect local sources for heating/cooling and wind stress. Although the effects of waves here were inconclusive, we can further speculate that wave-driven flow will affect the thermal exchange by determining residence times for water in shallow reef areas where wave-driven flow will dominate [e.g., *Hench et al*., 2008].

The flow regimes observed for the cross-shore flow at KNO are in sharp contrast to observations by *Monismith et al*. [2006] for a forereef environment in Eilat, Israel with similar heat fluxes, where the advective terms were shown to dominate. In that case, the reef slope was considerably steeper (1 in 5) which increases the ratio of advective to unsteady terms as noted in section 2. We can anticipate that variations in

slope, bed roughness, alongshore tidal forcing, wind stress and wave climate (among others) between different tropical reef coastlines will result in varied dynamic responses. Even at specific locations, we can anticipate cross-shore variations in dynamic regimes as suggested by the scaling discussion in section 2. The steady (advective) thermal response at Eilat, for example, would necessarily transition to an unsteady balance in deeper water. For KNO, we expect that the regimes observed at the 12 m isobath will apply over the nearshore region, but the dynamic response will likely also vary offshore, as the role of bottom stress, for example, becomes less pronounced.

**Acknowledgments**

Kilo Nalu received support from NSF CoOP project OCE-0536616 and NOAA project NA07NOS4730207 and from the City and County of Honolulu. The work presented here was carried out with support from NSF project OCE-0824832. We would like to express our gratitude to the staff at Kilo Nalu especially Kimball Millikan and Brian McLaughlin. The KNO buoy data were made possible due to the efforts of Eric DeCarlo and his staff. The analysis and interpretations benefited considerably from conversations with Antonio Sanchez, Liv Herdman, and Kristen Davis. Comments from three anonymous reviewers were also extremely helpful in improving the paper. KNO data are available by contacting G. Pawlak or via PacIOOS.

## References

Alford, M., M. Gregg, and M. Merrifield (2006), Structure, propagation and mixing of energetic baroclinic tides in Mamala Bay, Oahu, Hawaii, *J. Phys. Oceanogr.*, *36*, 997–1018.

Boden, B. (1952), Natural conservation of insular plankton, *Nature*, *169*, 697–699.

Cormack, D. E., G. P. Stone, and L. G. Leal (1975), The effect of upper surface conditions on convection in a shallow cavity with differentially heated end-walls, *Int. J. Heat Mass Transfer*, *18*, 635–648.

Cowen, R., and S. Sponaugle (2009), Larval dispersal and marine population connectivity, *Annu. Rev. Mar. Sci.*, *1*, 443–466.

Eich, M., M. Merrifield, and M. Alford (2004), Structure and variability of semidiurnal internal tides in Mamala Bay, Hawaii, *J. Geophys. Res.*, *109*, C05010, doi:10.1029/2003JC002049.

Fairall, C., E. Bradley, D. Rogers, J. Edson, and G. Young (1996), Bulk parameterization of air-sea flux for tropical ocean-global atmosphere coupled-ocean atmosphere response experiment, *J. Geophys. Res.*, *101*, 3747–3764.

Farrow, D. E. (2004), Periodically forced natural convection over slowly varying topography, *J. Fluid Mech.*, *508*, 1–21.

Farrow, D. E. (2013), Periodically driven circulation near the shore of a lake, *Environ. Fluid Mech.*, *13*, 243–255, doi:10.1007/s10652-012-9261-4.

Farrow, D. E., and J. C. Patterson (1993), On the response of a reservoir sidearm to diurnal heating and cooling, *J. Fluid Mech.*, *246*, 143–161.

Fer, I., U. Lemmin, and S. A. Thorpe (2002), Winter cascading of cold water in Lake Geneva, *J. Geophys. Res.*, *107*(C6), doi:10.1029/2001JC000828.

Fewings, M., and S. J. Lentz (2010), Momentum balances on the inner continental shelf at martha's vineyard coastal observatory, *J. Geophys. Res.*, *115*, C12023, doi:10.1029/2009JC005578.

Fewings, M., S. J. Lentz, and J. Fredericks (2008), Observations of cross-shelf flow driven by cross-shelf winds on the inner continental shelf, *J. Phys. Oceanogr.*, *38*, 2358–2378.

Fung, I., D. Harrison, and A. Lacis (1984), On the variability of the net longwave radiation at the ocean surface, *Rev. Geophys.*, *22*, 177–193.

Genin, A., S. Monismith, M. Reidenbach, G. Yahel, and J. Koseff (2009), Intense benthic grazing of phytoplankton in a coral reef, *Limnol. Oceanogr. Methods*, *54*, 938–951.

Grant, W. D., and O. S. Madsen (1979), Combined wave and current interaction with a rough bottom, *J. Geophys. Res.*, *84*, 1797–1808.

Hasselmann, K. (1970), Wave driven inertial oscillations, *Geophys. Fluid Dyn.*, *1*, 463–502.

Hatcher, B. G. (1997), Coral reef ecosystems: How much greater is the whole than the sum of the parts?, *Coral Reefs*, *16*, S77–S91.

Hench, J. L., J. Leichter, and S. Monismith (2008), Episodic circulation and exchange in a wave-driven coral reef and lagoon system, *Limnol. Oceanogr. Methods*, *53*, 2681–2694.

Horsch, G. M., and H. G. Stefan (1988), Circulation in littoral water due to surface cooling, *Limnol. Oceanogr.*, *33*(5), 1068–1083.

Huyer, A. (1976), A comparison of upwelling events in two locations: Oregon and Northwest Africa, *J. Mar. Res.*, *34*, 531–546.

Jones, N. L., R. J. Lowe, G. Pawlak, D. A. Fong, and S. G. Monismith (2008), Plume dispersion on a fringing coral reef system, *Limnol. Oceanogr. Methods*, *53*(5 part 2), 2273–2286.

Kellogg, C. A., J. B. Rose, S. Jaing, J. M. Thurmond, and J. H. Paul (1995), Genetic diversity of related vibriophages isolated from marine environments around Florida and Hawaii, USA, *Mar. Ecol. Prog. Ser.*, *120*, 89–98.

Lei, C., and J. C. Patterson (2002), Unsteady natural convection in a triangular enclosure induced by the absorption of radiation, *J. Fluid Mech.*, *460*, 181–209.

Lei, C., and J. C. Patterson (2005), Unsteady natural convection in a triangular enclosure induced by surface cooling, *Int. J. Heat Fluid Flow*, *26*, 307–321.

Leichter, J. J., S. Wing, S. Miller, and M. Denny (1996), Pulsed delivery of subthermocline water to Conch Reef (Florida Keys) by internal tidal bores, *Limnol. Oceanogr.*, *41*, 1490–1501.

Leopold, L. (1948), Diurnal weather patterns on Oahu and Lanai, Hawaii, *Pac. Sci.*, *2*, 81–95.

Monismith, S. G., and D. Fong (2004), A note on the potential transport of scalars and organisms by surface waves, *Limnol. Oceanogr. Methods*, *49*, 1214–1217.

Monismith, S. G., J. Imberger, and M. L. Morison (1990), Convective motions in the sidearm of a small reservoir, *Limnol. Oceanogr.*, *35*(8), 1676–1702.

Monismith, S. G., A. Genin, M. Reidenbach, G. Yahel, and J. Koseff (2006), Thermally driven exchanges between a coral reef and the adjoining ocean, *J. Phys. Oceanogr.*, *36*, 1332–1347.

Paul, J. H., J. B. Rose, S. C. Jiang, P. London, X. Xhou, and C. Kellogg (1997), Coliphage and indigenous phage in Mamala Bay, Oahu, Hawaii, *Appl. Environ. Microbiol.*, *63*, 133–138.

Pawlak, G., et al. (2009), Development, deployment, and operation of Kilo Nalu Nearshore Cabled Observatory, in *IEEE OCEANS 2009 Conference*, pp. 1–10, IEEE, Bremen, Germany.

Phillips, O. M. (1966), On turbulent convection currents and the circulation of the Red Sea, *Deep Sea Res. Oceanogr. Abstr.*, *13*, 1149–1160.

Price, J. F., R. A. Weller, and R. Pinkel (1986), Diurnal cycling: Observations and models of the upper ocean response to diurnal heating, cooling, and wind mixing, *J. Geophys. Res.*, *91*, 8411–8427.

Sevadjian, J., M. A. McManus, and G. Pawlak (2010), Effects of physical structure and processes on thin zooplankton layers in Mamala Bay, Hawai'i, *Mar. Ecol. Prog. Ser.*, *409*, 95–106.

Sturman, J. J., C. E. Oldham, and G. N. Ivey (1999), Steady convective exchange flows down slopes, *Aquat. Sci.*, *61*, 260–278.

Symonds, G., and R. Gardiner-Garden (1994), Coastal density currents forced by cooling events, *Cont. Shelf Res.*, *14*, 143–157.

Wells, J., J. P. Fram, and G. Pawlak (2012), Solar warming of near bottom water over a fringing reef, *J. Mar. Res.*, *70*, 641–660.